PCCP

ROYAL SOCIETY OF CHEMISTRY

PAPER

View Article Online
View Journal | View Issue

Cite this: *Phys. Chem. Chem. Phys.*, 2022, **24**, 28984

Theoretical study of the CO_2–O_2 van der Waals complex: potential energy surface and applications†

Yosra Ajili,[a] Ernesto Quintas-Sánchez,[b] Bilel Mehnen,[c] Piotr S. Żuchowski,[c] Filip Brzęk,[c] Nayla El-Kork,[d] Marko Gacesa,[d] Richard Dawes[b] and Majdi Hochlaf*[e]

A four-dimensional-potential energy surface (4D-PES) of the atmospherically relevant carbon dioxide–oxygen molecule (CO_2–O_2) van der Waals complex is mapped using the *ab initio* explicitly correlated coupled cluster method with single, double, and perturbative triple excitations (UCCSD(T)-F12b), and extrapolation to the complete basis set (CBS) limit using the cc-pVTZ-F12/cc-pVQZ-F12 bases and the l^{-3} formula. An analytic representation of the 4D-PES was fitted using the method of interpolating moving least squares (IMLS). These calculations predict that the most stable configuration of CO_2–O_2 complex corresponds to a planar slipped-parallel structure with a binding energy of $V \sim -243$ cm^{-1}. Another isomer is found on the PES, corresponding to a non-planar cross-shaped structure, with $V \sim -218$ cm^{-1}. The transition structure connecting the two minima is found at $V \sim -211$ cm^{-1}. We also performed comparisons with some CO_2–X van der Waals complexes. Moreover, we provide a SAPT analysis of this molecular system. Then, we discuss the complexation induced shifts of CO_2 and O_2. Afterwards, this new 4D-PES is employed to compute the second virial coefficient including temperature dependence. A comparison between quantities obtained in our calculations and those from experiments found close agreement attesting to the high quality of the PES and to the importance of considering a full description of the anisotropic potential for the derivation of thermophysical properties of CO_2–O_2 mixtures.

Received 3rd September 2022,
Accepted 16th November 2022

DOI: 10.1039/d2cp04101d

rsc.li/pccp

I. Introduction

In Earth's atmosphere, carbon dioxide is present in gaseous form under normal pressure and temperature conditions. It is the fourth most abundant gas there (~0.035%). At low temperatures, it can also be found in liquid and solid forms. Its supercritical fluid form is used for industrial extraction applications where it replaces hazardous liquids. Dioxygen, is the second most abundant gas in Earth's atmosphere (~21%), where it is in the gas phase under normal conditions. Industrially, O_2 is purified by the distillation of liquid air. It is used as an oxidizer, for medical purposes, and in a wide range of domestic and industrial combustion reactions. Dioxygen is also produced by living organisms through photosynthesis and is essential for the breathing process of most living organisms. In addition, thermophysical properties of carbon dioxide and dioxygen molecules are relevant for modeling Earth's atmosphere and the atmospheres of other celestial bodies and planets where these species are present such as Mars, Europa and Ganymede, as well as exoplanets. In a planetary atmosphere, CO_2 acts both as a powerful greenhouse gas and as a coolant, strongly influencing the formation and evolution of primary and secondary atmospheres of hot gas giants and terrestrial planets.[1,2] Very recently, CO_2 has been detected in transmission spectra in the atmosphere of the gas giant exoplanet WASP-39b,[3] confirming the hints of earlier photometric detections of CO_2 during transits.[4] Accurate photochemical modeling of CO_2-rich atmospheres of exoplanets will require detailed descriptions of thermophysical properties of carbon dioxide and other atmospheric species, such as dioxygen molecules.

Previous studies of molecular dimers whose interactions are already described in the literature are often in the form of multi-dimensional potential energy surfaces (PESs), describing

[a] *Université de Tunis El Manar, Faculté des Sciences de Tunis, LR01ES09 Spectroscopie Atomique et Moléculaire et Applications, 1060, Tunis, Tunisia*
[b] *Department of Chemistry, Missouri University of Science and Technology, Rolla, MO 65409-0010, USA*
[c] *Institute of Physics, Faculty of Physics, Astronomy and Informatics, Nicolaus Copernicus University, Grudziadzka 5, 87-100 Torun, Poland*
[d] *Space and Planetary Sciences Center, and Department of Physics, Khalifa University, P.O. Box 127788, Abu Dhabi, United Arab Emirates*
[e] *Université Gustave Eiffel, COSYS/IMSE, 5 Bd Descartes 77454, Champs sur Marne, France. E-mail: majdi.hochlaf@univ-eiffel.fr*

† Electronic supplementary information (ESI) available. See DOI: https://doi.org/10.1039/d2cp04101d

the potential energy for the full range of angular poses and interaction distances, usually with fixed monomer geometries. These multi-dimensional PESs are crucial to compute and interpret the spectroscopic and thermophysical properties of mixtures. Indeed, they are needed for the derivation of the rovibrational spectra of the complexes[5–8] or for inelastic energy transferring collisions[9] and are usually used for the derivation of the macromolecular thermophysical properties (*e.g.*, virial coefficients) of the dimer mixtures. Therefore, an accurate PES of the CO_2–O_2 van der Waals (vdW) complex is needed in order to predict and understand the spectroscopy and dynamical behavior of this system in various environments. In atmospheric and environmental contexts, systems composed of CO_2 interacting with small gas phased molecules are considered as prototypes, allowing extensive characteristic studies of the intermolecular interactions and molecular dynamics of vdW systems. Moreover, the CO_2–O_2 PES is of great importance for climate simulations since for CO_2–O_2, collision-induced-absorption is in the spectral ranges of atmospheric windows.

To date, there are numerous theoretical and experimental studies dedicated to vdW complexes involving CO_2 as well as O_2 with other molecules such as CO_2–O_2,[10–12] O_2–O_2,[11,13] O_2–N_2,[14] O_2–N_2O,[4,15] CO_2–H_2,[16] CO_2–CO_2,[5,17] CO_2–N_2,[18,19] CO_2–CO,[6,18,20] and CO_2–N_2O.[21] To the best of our knowledge, no analytical function of the CO_2–O_2 PES is available in the literature. In fact, information on this complex is limited to the recent works by Grein,[10] Madajczyk *et al.*,[11] and Lee *et al.*[12] In 2017, Grein used the explicitly correlated coupled cluster method in conjunction with the cc-pVXZ-F12 and the aug-cc-pVXZ (X = D up to Q) basis sets to identify some stationary points, where he used the RCCSD(T)-F12a approach for geometry optimizations while he employed the UCCSD(T)/aug-cc-pVDZ level for harmonic frequencies calculations. Grein found two minima and one T-shaped stationary point that was assigned in that paper to be a first-order saddle connecting them. These structures are shown in Fig. 1 and are labeled GM, LM, and TS2′. Later on, Madajczyk *et al.*[11] performed extensive methodological benchmarks on CO_2–O_2 interaction energies for the stationary points found by Grein. With the benefit of a complete 4D mapping, we find, however, that TS2′ is in fact one of three second-order saddles, as it is unstable with respect to an out-of-plane rotation of O_2, leading to the cross-shaped LM, but also with respect to a disrotatory in-plane geared motion leading to the slipped parallel GM. We do report one transition structure (a non-planar first-order saddle) connecting GM and LM. The topography of the PES and paths connecting critical points will be discussed in more detail later.

Experimentally, Lee *et al.*[12] used the CO_2–O_2 neutral vdW complex to show that electron attachment may lead to the formation of a monomeric molecular anion $(O_2–CO_2)^-$, which is an isomer of the gaseous anionic species $(CO_4)^-$. This anion is present in the ionosphere, with a newly formed C–O bond facilitating extensive delocalization of the free electron. Indeed, a significant bonding interaction was characterized resulting from the formation of the $(O_2–CO_2)^-$ monomeric anionic complex instead of the weak bond of the CO_2–O_2 vdW neutral system. Lee *et al.*[12] also reported some calculations at the MP2/6-311+G* level which predict an out-of-plane structure for the GM of the neutral CO_2–O_2 complex. The much higher-level calculations reported here are expected to be more reliable.

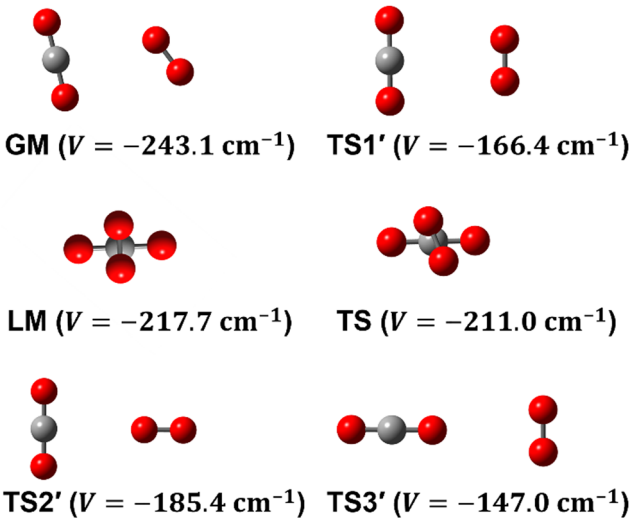

Fig. 1 Structures of the most relevant critical points of the CO_2–O_2 complex. The planar global minimum (GM) is connected to the cross-shaped local minimum (LM) along a path that passes through a transition structure (TS). Three planar second-order saddles are also noted (TS1′, TS2′, TS3′).

In this paper, we generate the 4D-PES of the CO_2–O_2 vdW complex describing the intermolecular coordinates. The electronic structure calculations are performed at the UCCSD(T)-F12b/CBS level of theory. An analytical expression of the PES was constructed and used to characterize the interactions and also to compute the temperature dependent second virial coefficient. We also provided rationalization of the shape of the PES using the energy decomposition provided by the Symmetry Adapted Perturbation Theory (SAPT) for high-spin open-shell complexes.[22–24] Moreover, we discuss the complexation-induced effects on the vibrational frequencies of the CO_2 and O_2 monomers. The paper is organized as follows: In Section II, we give details about the electronic structure calculations, the fitting methodology and analytical representation developed in this work. In Section III, we describe the main features of the PES. In Section IV, we discuss the monomers' vibrational frequencies either isolated or in CO_2–O_2 complexes and their shifts. Then, we compute the CO_2–O_2 mixture second virial coefficient in the 200–550 K temperature range and compare with available experiments. Good agreement between our theoretical data and the experimental measurements is observed although there is significant variation found in the various experiments which span several decades. This validates the 4D-PES and demonstrates its relevance for the deduction of thermophysical properties.

II. Interaction potential of the CO_2–O_2 complex

1. Electronic structure calculations

As depicted in Fig. 2, the coordinates used to represent the four-dimensional (4D) CO_2–O_2 PES ($V(R,\theta_1,\theta_2,\phi)$) are the Jacobi

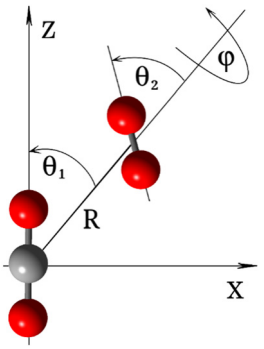

Fig. 2 Jacobi coordinates of the CO_2–O_2 complex.

coordinates: R, θ_1, θ_2 and ϕ. R is the distance between the centers of mass of the two fragments; θ_1 and θ_2 correspond to the angles between R and the molecular axes of the CO_2 and O_2 molecules, respectively; and ϕ denotes the dihedral (out of plane) torsional angle. For the construction of the PES, both monomers were held rigid. It is a good approximation in this application to consider only the inter-monomer coordinates because their frequencies are much less than those of the intra-monomer coordinates. The geometry of the O_2 molecule was held at equilibrium, using the vibrationally averaged distance: r_{OO} = 1.20752 Å, which is consistent with its experimental rotational constant.[25] The CO_2 molecule is held linear, with each CO bond-distance fixed at 1.162086 Å,[26] which is also consistent with its experimental rotational constant.[26,27]

The ground state of the CO_2–O_2 complex correlates to the CO_2 ($X^1\Sigma_g^+$) + O_2 ($X^3\Sigma_g^-$) dissociation limit at infinite inter-monomer separations. It has an open shell wavefunction of triplet spin multiplicity. Thus, the final high-level PES was computed using explicitly-correlated unrestricted coupled-cluster theory,[28] extrapolated to the complete basis set limit, UCCSD(T)-F12b/CBS. For the description of the atoms, we used the explicitly correlated basis sets (cc-pVXZ-F12) by Peterson and co-workers[29] and corresponding density fitting and resolution of identity basis sets as implemented in MOLPRO electronic structure code package.[30] The basis extrapolation was performed using the cc-pVTZ-F12 and cc-pVQZ-F12 bases and the l^{-3} formula.[31] All *ab initio* calculations were performed using MOLPRO.

In our experience with dimer complexes composed of a few light atoms, the binding energy and relative energies of vdW isomers are typically converged to within a few wavenumbers with this procedure, which does not employ counterpoise corrections or mid-bond functions. Indeed, we tested the effect of adding mid-bond functions for this system and find the impact to be negligible at the CBS level, affecting the well-depth at the GM by only 1.4 cm^{-1} and less in other regions. At the triple-zeta level, however, the results obtained without mid-bond functions are significantly better (closer to CBS) than those obtained with mid-bond functions. Careful testing for a particular system, method, and basis set seems warranted when considering use of mid-bond functions. Stable convergence to the restricted open-shell Hartree–Fock (ROHF) reference was achieved by first using MOLPRO's CASSCF (multi) algorithm with the occupation of the desired configuration specified, followed by a single iteration of the ROHF SCF algorithm to prepare the orbitals for the UCCSD(T)-F12b procedure. As mentioned below, to avoid placing expensive high-level data in energetically inaccessible regions, a lower-level guide surface was first constructed. This was done using data at the UCCSD(T)-F12a/cc-pVDZ-F12 level of theory. The guide surface is only used to aid in the efficient construction of the high-level PES, on which all evaluations used to study the dynamics were performed. Exploiting the system's symmetry, energies were only computed in the reduced angular range: $0^\circ < \theta_1 < 90^\circ$, $0^\circ < \theta_2 < 90^\circ$, and $0^\circ < \phi < 180^\circ$.

2. Analytical potential function

As we have done in the past for other vdW linear dimers[32–39] an analytical representation of the 4D-PES was constructed using an automated interpolating moving least squares (IMLS) methodology, freely available as a software package under the name AUTOSURF.[40] As usual,[41,42] a local fit was expanded about each data point, and the final potential is obtained as the normalized weighted sum of the local fits. The fitting basis and other aspects of the procedure were the same as for other previous systems and have been described in detail elsewhere.[40,42,43] The shortest inter-monomer center-of-mass distance considered is R = 2.0 Å and the *ab initio* data coverage in the fitted PES extends to R = 16.0 Å, while the zero of energy is set at infinite center-of-mass separation between the monomers. For the high-level 4D-PES, 1438 symmetry-unique points were required to achieve an estimated root-mean-squared fitting error of 0.3 cm^{-1} for energies below the asymptote. As discussed in previous applications of our approach, since the fit is interpolative and thus passes through each included data point, a straightforward RMS error measure isn't applicable. The fit quality is therefore estimated by other means including use of independent test sets.[42] The 4D-PES switches to an analytical form describing the long range based on the leading electrostatic (quadrupole–quadrupole) and dispersion terms, which vary as R^{-5} and R^{-6} respectively. For consistency, the parameters of the long-range form were determined by a least squares fit to the subset of *ab initio* data with $R > 8.0$ Å. To guide the placement of high-level data, a lower-level guide surface was constructed using 1370 symmetry-unique points, distributed using a Sobol sequence[44] biased to sample the short range region more densely. This PES will be sent upon request.

III. Description of the 4D-PES

Some of us have been involved in the construction of each of a large number vdW PESs for which both monomers are linear and hence the intermolecular interactions are 4D. These include: $(OCS)_2$,[45] $(CO)_2$,[46] $(CO_2)_2$,[5,47] CO_2–CO,[6,32] CO_2–CS_2,[48] CO–N_2,[49] $(NNO)_2$,[50] CO_2–HCCH,[51] C_6H^-–H_2,[52] HC_2NC–H_2,[53] O_2–CO,[54] O_2–HCl, O_2–HF, H_2–O_2, O_2–N_2,[37,55] CO–HCCH, HNC_3–H_2,[53] HC_5N–H_2,[53] C_4H^-–H_2,[38] C_2H^-–H_2, $MgCCH$–H_2,

CF^+–H_2,[33] HCS^+–H_2,[39] NCCP–H_2, PN–H_2,[36] CO_2–N_2,[8,19,35] and O_2–O_2.[56,57] Four systems from that list include CO_2, and six others include O_2. Except for the cases of ions, whose PESs typically have simpler topographies, the rich and subtle balance of possible steric and electronic interactions as well as symmetry considerations, give rise to a complex variety of predicted isomers, transition structures, and connecting paths. Many of the isomers are planar and include configurations such as slipped- or skewed-parallel or anti-parallel (in some cases non-polar due to structure and symmetry), T-shaped or nearly T-shaped, with either end of each fragment possibly stabilized when pointing towards the side of the other molecule. Colinear, or slightly skewed nearly colinear arrangements are sometimes observed. Non-planar isomers are also common and are often accompanied by planar isomers. These usually take the form of perfect cross shapes, although they are sometimes slightly skewed in one or more coordinates. Symmetry can play a role. Remarkably, what is a local or even global minimum geometry in one system can be quite unstable and perhaps a saddle point of some order in another.

Once the 4D-PES has been constructed, it is insightful to generate some plots such as those in Fig. 3. With the torsion fixed at ϕ = 0 degrees (enforcing planar geometries) a 2D plot was made for the complete ranges of both θ_1 and θ_2. At each point on the plot corresponding to a pair of (θ_1, θ_2) values, the energy is minimized with respect to R. Thus, any planar isomers, transition structures, and paths between them are represented, all fully relaxed. Optionally, in the same fashion, an extended angles plot can be constructed allowing each fragment to rotate a full 360°. This doesn't provide additional information for this system given its symmetry, but can facilitate viewing of paths that otherwise exit the plot on one side and re-emerge on the other. The left panel of Fig. 3 shows the two symmetry equivalent wells corresponding to the global minimum (GM). From GM, rotation mostly of one fragment or the other leads to the two possible T-shaped structures in this system (one for each monomer acting as the stem of the T). These are TS2′ (O_2 as the stem) and TS3′ (CO_2 as the stem), found in the middle of the plot borders, top/bottom and left/right respectively. They each appear twice due to symmetry. These are 2nd-order saddles since they are unstable to in-plane rotation of the stem fragment, leading back to GM, but also with respect to out-of-plane stem fragment rotation leading to the cross minimum. The right side of Fig. 3 shows the same type of plot, but with the torsion fixed at ϕ = 90°, which includes the cross-shaped minimum. The torsion angle is undefined for a precise T-shaped structure but TS2′ and TS3′ are shown on the edges of both plots. The side-by-side parallel structure (TS1′) appears in the center of the ϕ = 0° plot, and although labeled a transition state by Grein is shown here to be a 2nd-order saddle. It is unstable with respect to a geared disrotatory in-plane motion leading to GM, and also with respect to rotation in ϕ, leading to the cross-shaped LM. A thorough search through similar optimized plots for a sequence of values of ϕ, enabled location of the TS connecting GM and LM. Fig. 4 plots this path in ϕ, with the other three coordinates relaxed at each point, locating the TS at ϕ = 70.5°. GM and LM differ significantly in terms of R (geometric parameters are given in Table 1), with LM found at a shorter separation (R = 3.20 Å for LM compared with R = 3.38 Å for GM). The value of R for the TS is already close to that of LM, at R = 3.24 Å. A closer look at geometries along the path between

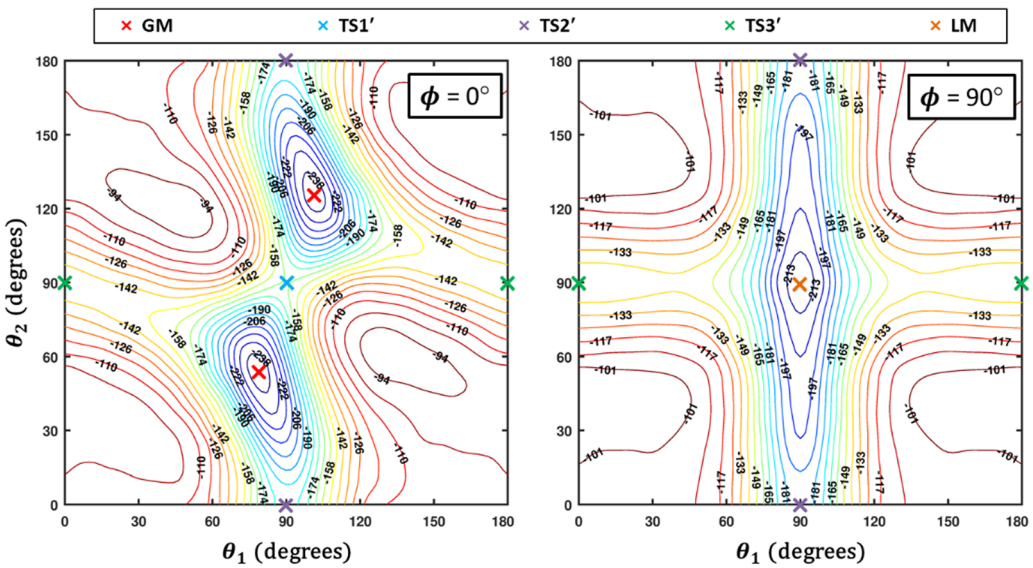

Fig. 3 R-Optimized contour plots of the CO_2–O_2 4D-PES as a function of θ_1 and θ_2 for (at left) the planar (ϕ = 0°) geometries, and (at right) the non-planar (ϕ = 90°) geometries. For each pair of angles (θ_1, θ_2), the energy is minimized by varying R. The global minimum (GM) and its symmetry partner appear in the ϕ = 0° plot at left, while the local cross-shaped minimum (LM) is found in the ϕ = 90° plot. Symmetry partners of the three second-order saddles (structures given in Fig. 1) are also indicated on the plots. The TS connecting GM and LM does not appear since ϕ = 70.5° for that structure (see Fig. 4).

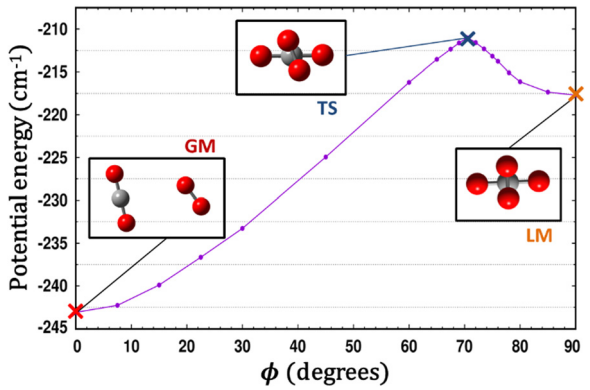

Fig. 4 A scan along ϕ with all three of the other coordinates optimized at each point illustrates the path connecting the global minimum (GM) and the local minimum (LM) which passes through a TS.

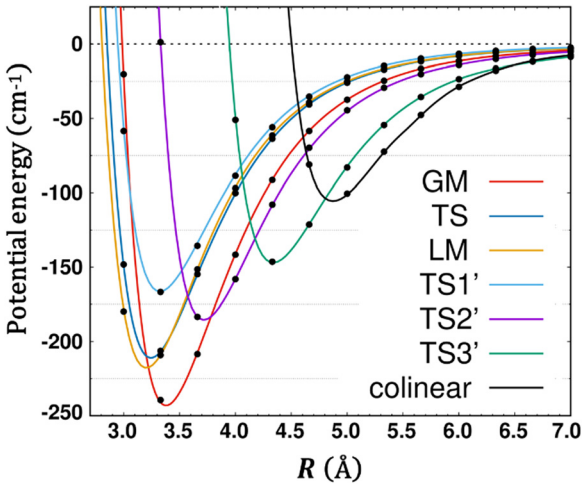

Fig. 5 Seven radial cuts are presented which reveal the strong anisotropy of the PES. Angular poses correspond to approach through each of the 6 critical points shown in Fig. 1 as well as the end-on colinear orientation. Lines plot the fitted PES, while points represent *ab initio* data (not used in the fit).

GM and LM reveals that θ_2 changes more significantly than θ_1, and it is when ϕ increases from about 50–70°, that θ_2 changes the most and R contracts correspondingly.

Fig. 5 presents radial 1D-cuts of the 4D-PES passing through each of the critical points identified in this study. The strong anisotropy is highlighted as minima in R appear at a wide range of values for the various angular poses. Fig. 5 also confirms the fitting accuracy of the 4D-PES as a number of *ab initio* data that were not included in the fit are plotted along each radial slice and closely match the fitted values.

Fig. 3 and 4 imply that a complex manifold of rovibrational levels can be anticipated, even before considering the effect of electronic spin. Nuclear spin statistics will dictate allowed levels and transitions for the various isotopologues. Tunneling splittings due to symmetry partners of GM are expected, and substantial delocalization and perturbation of even low-lying levels are likely. As seen in the left side of Fig. 3, exploration from GM toward the T-shaped TS2′ can occur with little necessary energy. The right side of Fig. 3 highlights the fact that for the cross-shaped LM, the complex is extremely floppy with respect to θ_2, motion of the O_2 fragment. Fig. 4 shows that the barrier between GM and LM is low and thus interference between the stacks of levels is possible, although, similar to the case of $(CO)_2$,[46] the isomers can be distinguished by their rather different center-of-mass distances (see Table 1). For SN–H$^-$,[58] SH–N$^-$[58] and CO_2–N_2[8] weakly bound complexes, quantum effects, such as tunneling, vibrational memory, and localization effects were predicted. A previous study of CO–O_2 indicates that although the electronic spin adds additional complexity in these triplet systems, a great deal of useful insight and interpretation of the experiments can be made even while neglecting the spin term.[54]

It is remarkable to consider the variety of interactions and resulting isomers for complexes of CO_2 with other partners including itself. The interactions vary significantly in strength as well as with respect to orientation. For example, the GM of the CO_2–N_2O[21] complex has a similar shape as GM of CO_2–O_2, whereas no equivalent structure found in the CO_2–H_2,[59] CO_2–CO_2,[5,47] CO_2–N_2,[8,19,35] or CO_2–CO[6,18,20,32] PESs. This can be interpreted in terms of orbital overlaps. The bonding for CO_2–O_2 GM and LM can be viewed as electron donation to the electropositive C of CO_2 from the lone pair of O_2 located in the π_g* molecular orbital (MO) of O_2, as illustrated in Scheme 1. For CO_2–H_2, CO_2–N_2 and CO_2–CO dimers, the outermost σ orbital of H_2/N_2/CO interacting with such C promotes T-shaped minima (either global or local, *cf.* Scheme 1), corresponding however to unfavorable interactions for CO_2–O_2 resulting in a transition state (*e.g.* TS2′, *cf.* Scheme 1). For $(CO_2)_2$, overlap between the outermost π MOs of CO_2 then promotes the global minimum slipped parallel form (θ_1 = 58.7°, θ_2 = 58.7°, ϕ = 0°), while the T-shape structure corresponds to a transition structure (*cf.* Scheme 1). Fig. 6 compares the CO_2–O_2 and CO_2–N_2 systems, both homonuclear diatomics and neighbors on the periodic table, but with very different electron configurations. The plots in Fig. 6 were obtained after scanning the out-of-plane rotation (θ_2) of N_2 or O_2, while holding θ_1 and ϕ fixed, and relaxing R at each point. The T-shaped global minimum for CO_2–N_2 corresponds to an unstable 2nd-order saddle for CO_2–O_2, while the cross-shaped LM for CO_2–O_2 becomes a TS for CO_2–N_2.

Table 1 Geometrical parameters (R in Å and angles in degrees) and energies (V in cm^{-1}) from the fitted 4D-PES are listed for the 6 structures shown in Fig. 1, as well as for the minimum energy colinear end-on arrangement. Radial cuts through the 4D-PES for all of these orientations are given in Fig. 5 (the torsion is undefined for T-shaped or colinear configurations)

Structure	GM	LM	TS	TS1′	TS2′	TS3′	colinear
R	3.379	3.202	3.244	3.325	3.717	4.339	4.873
θ_1	78.5	90.0	86.0	90.0	90.0	0.0	0.0
θ_2	55.0	90.0	79.0	90.0	0.0	90.0	0.0
ϕ	0.0	90.0	70.5	0.0	—	—	—
V	−243.1	−217.7	−211.0	−166.4	−185.4	−147.0	−105.5

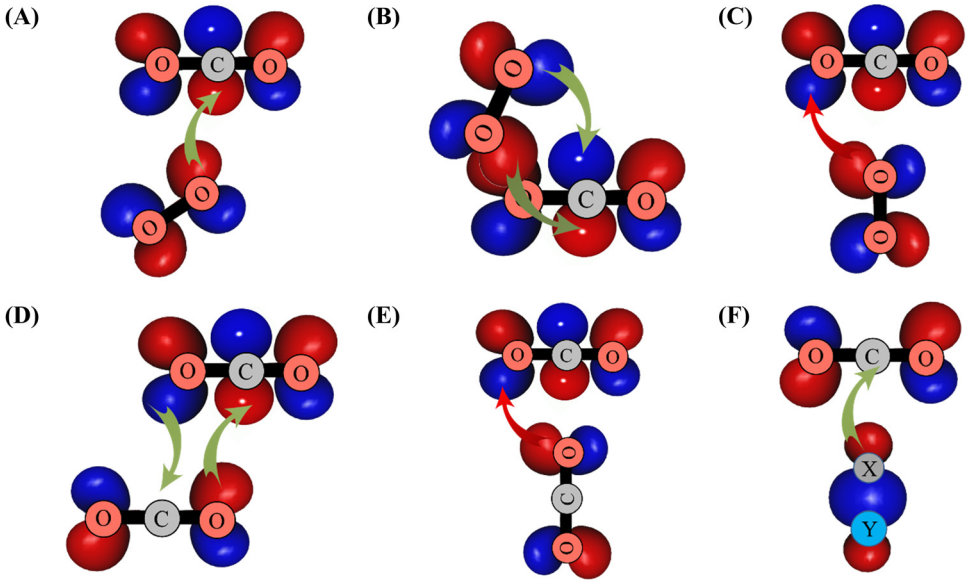

Scheme 1 Illustration of overlaps between the π_g* MO of O_2 and outermost π_u MO of CO_2 leading to the formation of GM (in (A)), of LM (in (B)) and of TS2′ (in (C)). The formation of the other CO_2–O_2 structures displayed in Fig. 1 can be obtained with similar considerations. In (D) and (E), we give the interactions between the CO_2 outermost orbitals resulting in the formation of the global and the T-shape transition structures of $(CO_2)_2$. In (F), we illustrate the overlap between the outermost σ MO of XY (XY = H_2 or N_2 or CO) and the outermost π_u MO of CO_2. π_g* (π_u) MO corresponds to the HOMO (LUMO) of O_2 (CO_2). σ MO is the HOMO of XY species. Favorable (unfavorable) overlaps are represented by green (red) arrows.

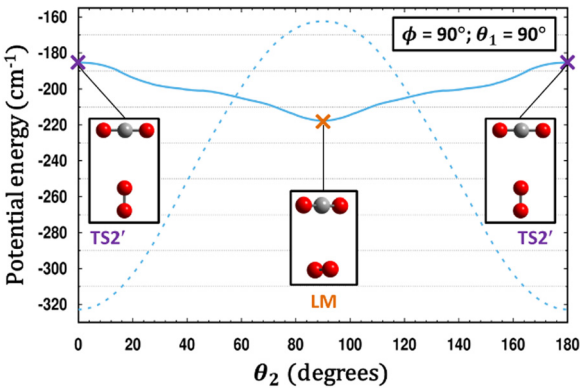

Fig. 6 A comparison is made between the PESs of CO_2–O_2 (solid line) and CO_2–N_2 (dashed line).[35] For each system, a scan of θ_2 is performed holding θ_1 and ϕ fixed, and for each value of θ_2, the energy in each case is minimized with respect to R. Remarkably, what is a T-shaped global minimum for CO_2–N_2 becomes an unstable 2nd-order saddle in CO_2–O_2, while the cross-shaped structure in the center of the plot at $\theta_2 = 90°$ is a local minimum for CO_2–O_2 yet a transition structure for CO_2–N_2.

The well depths for the global minima of some of the CO_2 bearing vdW complexes fall into the following order: CO_2–C_2H_2[51] > CO_2–N_2O[21] > CO_2–CO_2[5,47] > CO_2–CO[6,32] > CO_2–N_2[8,19,35] > CO_2–O_2 > CO_2–H_2,[59] with V (in cm^{-1}) = 751, 581, 520, 407, 323, 243, and 220, respectively. Most of these neutral partners are nonpolar and clearly the different electron configurations play a key role. The deepest global minimum from this set is for C_2H_2 (acetylene), which with its triple bond, positions itself into a close side-by-side parallel geometry at a distance of R = 3.20 Å (the same distance as the cross-shaped LM in CO_2–O_2). This is not a stable configuration in the other systems.

IV. SAPT analysis

We have used a SAPT implementation based on the psi4numpy[60] module of Psi4 suite of codes implemented by some of us with the density fitting approach.[61,62] The reference wavefunction for the first-order electrostatics and exchange energies correspond to the UHF level of theory, while for the dispersion energy we have used the RPA approximation.[63] We have performed the calculations using aug-cc-pVXZ basis sets (with X = T,Q)[64,65] with and without mid-bond functions.

The calculations using various basis sets were performed for GM, LM and TS2′ geometries obtained in the present paper. Results were gathered in Table 2. A brief comparison with values from Table 1 shows fairly good agreement of SAPT(RPA) compared to UCCSD(T)-F12 values from our fit. The interaction energy was defined as the sum of all contributions to the second order. A common practice for a non-polar system is to neglect contributions beyond second order which can be calculated as the difference between the Hartree–Fock interaction energy and the sum of SAPT correction obtained at Hartree–Fock level. This contribution is commonly denoted as δ_{HF} and is also shown in Table 2. At each of the tested critical points, dispersion energy is the main binding force, while the first-order exchange energy is the biggest repulsive factor.

Since the center-of-mass distance R is similar for the GM, LM and TS2′ stationary points, there are generally only small differences in the dispersion component between these cases. The most dramatic change originates from the electrostatic

Table 2 Components of the interaction energy derived from the SAPT(RPA) approach are listed for GM and LM, and TS2′. The energy unit is cm^{-1}. Plots for the 6 structures shown in Fig. 1 are given in Fig. S1 of the ESI

Geometry	Basis	E_{int}	$E^{(1)}_{elst}$	$E^{(1)}_{exch}$	$E^{(2)}_{ind}$	$E^{(2)}_{exch-ind}$	$E^{(2)}_{disp}$	$E^{(2)}_{exch-disp}$	δ_{HF}
GM	TZ	−219.86	−130.80	348.63	−143.09	103.25	−431.12	33.28	−11.95
	TZ+mb	−238.35	−130.26	348.51	−143.35	102.87	−452.93	36.81	−12.00
	QZ	−236.02	−131.31	348.55	−143.56	103.29	−448.78	35.78	−12.04
	QZ+mb	−247.44	−131.68	348.48	−143.88	103.37	−462.10	38.37	−12.08
LM	TZ	−175.91	−61.55	300.83	−113.93	88.06	−419.95	30.63	−8.86
	TZ+mb	−194.73	−59.84	300.48	−114.30	87.54	−442.49	33.88	−8.97
	QZ	−192.30	−60.89	300.82	−114.78	88.21	−438.66	33.01	−8.95
	QZ+mb	−204.11	−61.53	300.81	−115.14	88.22	−451.79	35.32	−8.99
TS2′	TZ	−145.22	−12.14	241.64	−85.41	67.57	−381.73	24.85	−9.75
	TZ+mb	−157.42	−9.03	241.32	−85.53	67.15	−398.55	27.22	−9.85
	QZ	−156.09	−9.10	241.19	−84.75	66.57	−396.75	26.75	−9.89
	QZ+mb	−165.51	−9.32	241.17	−85.05	66.65	−407.58	28.61	−9.91

interaction: in case of the secondary minimum (LM) the electrostatic energy is less than half of that at GM, and nearly zero in case of the T-shaped TS2′. This is somewhat expected as usually the electrostatic energy is the most anisotropic contribution even in the case of non-polar molecules. As is usually the case, the exchange-induction energy cancels out strongly with the induction energy, yet, the cancellation is not complete, thus the net overall effect of the induction forces is large compared to the interaction energy at these points: $\sim -40\ cm^{-1}$ in GM, $\sim -25\ cm^{-1}$ at LM and $\sim -19\ cm^{-1}$ at TS2′.

In Fig. S1 (ESI†), we show radial cuts through the 4D-PES corresponding to the GM, LM, TS, TS1′, TS2′, and TS3′ angular orientations. These plots confirm that the interaction energy originates mostly from the interplay between dispersion and exchange energies. In the case of the linear configuration, as expected, the steric Pauli repulsion is strongest, which manifests in the rapid increase of the exchange energy at a short range. For all geometries considered in this section, the induction-, electrostatics- and higher-order exchange energies along with δ_{HF} are small. As for the electrostatic interactions, this effect is repulsive at long range only for the parallel (TS1′, H-shape) configuration, and near the minima, the electrostatics are typically attractive. The induction forces quickly vanish with R and become very small: for quadrupole-quadrupole interactions, such decay is known to have R^{-8} asymptotic behavior, and a strong cancellation with exchange-induction energy occurs. Note also that in Ref. 57 similar character of the molecular interaction was reported for the quintet state of the O_2–O_2 system.

V. Applications

1. Complexation induced shifts

Upon complexation, modifications of the physico-chemical properties and of the geometries of the constituent monomers can occur. Regardless of the type of interaction involved, it is instructive to discuss the changes induced on the monomers within the complex. When experimental information on the complexes is not available, it is common to perform comparisons between the calculated data of the isolated monomers and those in within the complexes. Therefore, we give in Table 3 the (U)CCSD(T)-F12/aug-cc-pVTZ harmonic vibrational frequencies of isolated $O_2(X^3\Sigma_g^-)$ and $CO_2(X^1\Sigma_g^+)$ and those for GM and LM of the complex. For the monomers, we list also the corresponding experimental values, which compare reasonably to the calculated harmonic frequencies due to modest anharmonicity. The recorded errors are less than 1% for the equilibrium distances and less than 3% for the frequencies.

Table 3 shows that all monomer modes change by complexation. The shifts are more pronounced for GM than for LM.

Table 3 Harmonic frequencies (ω_i, in cm^{-1}) and equilibrium distances (in Å) of the free CO_2 and O_2 monomers in their electronic ground states and harmonic frequencies (ω_i, cm^{-1}) of the CO_2–O_2 complex as computed at the (U)CCSD(T)-F12/aug-cc-pVTZ level of theory, where all degrees of freedom were relaxed. We also give the assignment of the vibrational modes. Shifts are computed as the difference between the isolated and complexed monomer frequencies

	Bond length			
Monomer	Bond	Computed	Experimental	Error in %
$O_2(X^3\Sigma_g^-)$	R_{OO}	1.217	1.20752[a]	0.8
$CO_2(X^1\Sigma_g^+)$	R_{CO}	1.162	1.1621[b]	∼0

	Frequencies			
Monomer	Mode	Computed	Experimental[a]	Error in %
$O_2(X^3\Sigma_g^-)$	ω(OO)	1605.9	1580.19[a]	1.6
$CO_2(X^1\Sigma_g^+)$	$\omega_{sym\ stretch}$	1352.5	1388.17[b]	2.6
	$\omega_{bending}$	673.1	667.40[b]	0.8
	$\omega_{anti\ sym\ stretch}$	2393.2	2359.61[b]	1.4

	CO_2–O_2			
	GM		LM	
Mode	Frequencies	Shifts	Frequencies	Shifts
ω(OO)	1602.7	3.2	1604.1	1.8
$\omega_{CO_2\ sym\ stretch}$	1353.3	−0.8	1352.4	0.1
$\omega_{CO_2\ bending}$	671.3	1.8	672.2	0.9
$\omega'_{CO_2\ bending}$	672.9	0.2	672.9	0.2
$\omega_{CO_2\ anti\ sym\ stretch}$	2394.0	−0.8	2393.2	0

[a] Ref. 66. [b] Ref. 67.

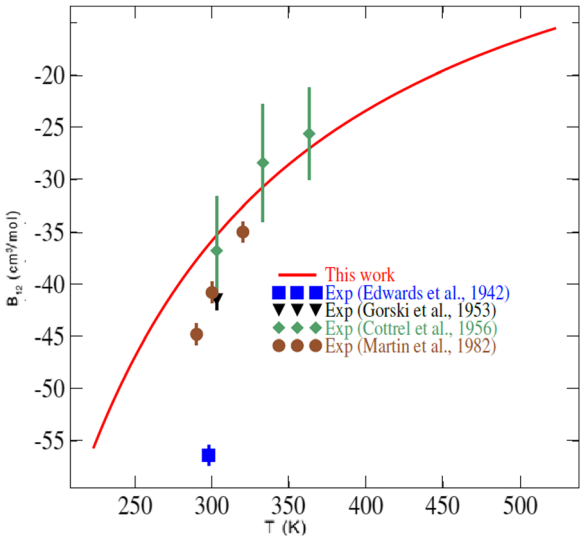

Fig. 7 Temperature dependence of the second virial coefficient of the CO_2–O_2 mixture. The symbols are experimental values (Exp.) found in the literature.[68–71]

This is consistent with the perturbation of the outermost π_g^* MO of CO_2 interacting with O_2 (see above). Also, the O_2 vibrational frequency is more affected than the CO_2 frequencies. Indeed, O_2 redshifts by 3.2 and 1.8 cm^{-1} in GM and LM, respectively. In particular, there is a lifting of degeneracy of the bending mode of CO_2: they redshift by 1.8 and 0.2 cm^{-1} (0.9 and 0.2 cm^{-1}) in GM (LM). In GM, the stretching modes of CO_2 blueshift, whereas they remain almost unchanged in LM. Note that these shifts are relatively significant, and they can be probed by IR spectroscopy of the complexes.

2. Second virial coefficients

To check the validity of our 4D-PES obtained with *ab initio* calculations, second virial coefficient computations were performed employing the fitted potential for the CO_2–O_2 complex. In the case of rigid molecules, the classical second virial coefficient, B, is expressed as a function of temperature as

$$B(T) = \frac{N_A}{2}\int\left(1 - \exp\left(-\frac{V(R,\Omega)}{kT}\right)\right)R^2 \mathrm{d}R\mathrm{d}\Omega \qquad (1)$$

where N_A is the Avogadro number, $V(R,\Omega)$ $(=V(R,\theta_1,\theta_2,\phi))$ is our 4D-PES. As indicated above, R is the distance between the two centers of mass corresponding to CO_2 and O_2 molecules and Ω is a set of angular coordinates $\{\theta_1,\theta_2,\phi\}$ defining all possible configurations corresponding to the O_2 orientation with respect to the CO_2 molecule.

In the literature, very few experimental data are available for the second virial coefficient of the CO_2–O_2 mixture to compare with. Indeed, no experimental data exist for temperatures lower than 250 K or temperatures higher than 400 K. Fig. 7 shows our results for the second virial coefficient and those values measured by Edwards and Roseveare,[68] Gorski and Miller,[69] Cottrell *et al.*,[70] and by Martin *et al.*[71] This figure shows generally good agreement between our calculations and the experimental values. While small discrepancies of 4 to 9 cm^3 mol^{-1} are found between our calculations and the experimental values of Gorski and Miller[69] from 1953, and the more recent measurements of Martin *et al.*,[71] excellent agreement is found with the measurements of Cottrell *et al.*[70] (1956). The early (1942) single value provided by Edwards and Roseveare[68] is discordant in the plot, deviating significantly from the other measurements and our calculations. It should be noted that the measurements of Edwards and Roseveare also deviate from the experimental consensus for other systems such as He–N_2,[72] N_2–H_2,[73] as well as from the CO_2–N_2 *ab initio* second virial coefficient calculations of Crusius *et al.*[74] The performance of the calculations attests to the high accuracy of our 4D-PES and to the utility of the explicitly correlated method for mapping multidimensional PESs for these applications.

VI. Conclusion

The potential interaction energies of the CO_2–O_2 vdW complex were generated *ab initio* as a function of the distance between the centers of mass of CO_2 and O_2 and the angular coordinates at the UCCSD(T)-F12/CBS level. This 4D-PES is strongly anisotropic. In addition to the stationary points found previously, we locate three additional critical points. Their binding energies and geometrical parameters were determined. SAPT analysis shows that the system is dominated mostly by the interplay between dispersion and first-order exchange forces. The relative changes of the electrostatic interaction upon the orientations of CO_2 and O_2 molecules are quite pronounced, and they strongly contribute to the overall anisotropy of the potential in the minimum region. Overall, the agreement of SAPT and UCCSD(T)-F12 methods is reasonable. We also report the complexation induced shifts of the vibrational modes of the monomers and the second virial coefficient of the CO_2–O_2 mixture for which good agreement with recent available experimental determinations is observed, which validates this new 4D-PES. This confirms the well-established performance of explicitly correlated methods for the generation of multidimensional potential energy surfaces and for their accurate description of polyatomic–polyatomic weakly bound vdW interactions.[7] These results extend our conclusions for previous polyatomic systems[5,6,8,75] to larger molecular systems for thermophysical properties calculations, and demonstrate the high quality of our interaction potentials.

Conflicts of interest

There are no conflicts to declare.

Acknowledgements

This study was carried out while M. H. was Visiting Professor at Khalifa University (supported by the internal grant 8474000362-KU-FSU-2021). M. G. is partly supported by Khalifa University (grants 8474000336-KU-SPSC and 8474000362-KU-FSU-2021).

N. E. K. is partly supported by Khalifa University (grants 8474000336-KU-SPSC and ASPIRE grant AARE20-031). R. D. and E. Q.-S. were supported by the U.S. Department of Energy (Award No. DE-SC0019740). B. M., P. Z. and F. B. acknowledge the National Science Center for support (Sonata Bis 9, Grant No. 2019/34/E/ST4/00407). We also acknowledge partial support from the Programme National ''Physique et Chimie du Milieu Interstellaire'' (PCMI) of CNRS/INSU with INC/INP co-funded by CEA and CNES.

References

1 K. Lodders and B. Fegley, *Icarus*, 2002, **155**, 393.
2 K. Zahnle, M. S. Marley, R. S. Freedman, K. Lodders and J. J. Fortney, *Astrophys. J. Lett.*, 2009, **701**, L20–L24.
3 E.-M. Ahrer, *et al.*, *Nature*, 2022, DOI: **10.1038/s41586-022-05269-w**.
4 J. J. Spake, *et al.*, *Mon. Not. R. Astron. Soc.*, 2021, **500**, 4042.
5 Y. N. Kalugina, I. A. Buryak, Y. Ajili, A. A. Vigasin, N.-E. Jaidane and M. Hochlaf, *J. Chem. Phys.*, 2014, **140**, 234310.
6 A. Badri, L. Shirkov, N.-E. Jaidane and M. Hochlaf, *Phys. Chem. Chem. Phys.*, 2019, **21**, 15871.
7 M. Hochlaf, *Phys. Chem. Chem. Phys.*, 2017, **19**, 21236.
8 M. Lara-Moreno, T. Stoecklin, P. Halvick and M. Hochlaf, *Phys. Chem. Chem. Phys.*, 2019, **21**, 3550; M. Lara-Moreno, T. Stoecklin, P. Halvick and M. Hochlaf, Erratum, *Phys. Chem. Chem. Phys.*, 2021, **23**, 10687.
9 E. Roueff and F. Lique, *Chem. Rev.*, 2013, **113**, 8906.
10 F. Grein, *Comput. Theor. Chem.*, 2017, **1114**, 101.
11 K. Madajczyk, P. S. Żuchowski, F. Brzęk, Ł. Rajchel, D. Kędziera, M. Modrzejewski and M. Hapka, *J. Chem. Phys.*, 2021, **154**, 134106.
12 S. H. Lee, N. Kim, T.-R. Kim, S. Shin and S. K. Kim, *J. Phys. Chem. A*, 2021, **125**, 5794.
13 M. Bartolomei, M. I. Hernandez, J. Campos-Martinez, E. Carmona-Novillo and R. Hernandez-Lamoneda, *Phys. Chem. Chem. Phys.*, 2008, **10**, 5374.
14 M. Bartolomei, E. Carmona-Novillo, M. I. Hernandez, J. Campos-Martinez and R. Moszynski, *J. Phys. Chem. Lett.*, 2014, **5**, 751.
15 S. R. Salmon and J. R. Lane, *J. Chem. Phys.*, 2015, **143**, 124303.
16 H. Ran, Y. Zhou and D. Xie, *J. Chem. Phys.*, 2017, **126**, 204304.
17 J. D. McMahon and J. R. Lane, *J. Chem. Phys.*, 2011, **135**, 154309.
18 K. M. de Lange and J. R. Lane, *J. Chem. Phys.*, 2011, **134**, 034301.
19 S. Nasri, Y. Ajili, N.-E. Jaidane, Y. N. Kalugina, P. Halvick, T. Stoecklin and M. Hochlaf, *J. Chem. Phys.*, 2015, **142**, 174301.
20 S. Sheybani-Deloui, A. J. Barclay, K. H. Michaelian, A. R. W. McKellar and N. Moazzen-Ahmadi, *J. Chem. Phys.*, 2015, **143**, 121101.
21 L. Zheng, S.-Y. Lee, Y. Lu and M. Yang, *J. Chem. Phys.*, 2013, **138**, 044302.
22 B. Jeziorski, R. Moszynski and K. Szalewicz, *Chem. Rev.*, 1994, **94**, 1887.
23 P. S. Żuchowski, R. Podeszwa, R. Moszyński, B. Jeziorski and K. Szalewicz, *J. Chem. Phys.*, 2008, **129**, 084101.
24 M. Hapka, P. S. Żuchowski, M. M. Szczęśniak and G. Chałasiński, *J. Chem. Phys.*, 2012, **137**, 164104.
25 C. Amiot and J. Verges, *Can. J. Phys.*, 1981, **59**, 1391.
26 G. Guelachvili, *J. Mol. Spectrosc.*, 1980, **79**, 72.
27 H. Li, P.-N. Roy and R. J. Le Roy, *J. Chem. Phys.*, 2010, **132**, 214309.
28 G. Knizia and T. B. Adler, *J. Chem. Phys.*, 2009, **130**, 054104.
29 K. A. Peterson, T. B. Adler and H.-J. Werner, *J. Chem. Phys.*, 2008, **128**, 084102.
30 H. J. Werner, P. J. Knowles, G. Knizia, F. R. Manby and M. Schütz, Molpro: a generalpurpose quantum chemistry program package, *Wiley Interdiscip. Rev.: Comput. Mol. Sci.*, 2012, **2**, 242–253.
31 D. Feller, K. A. Peterson and T. D. Crawford, *J. Chem. Phys.*, 2006, **124**, 054107.
32 E. Castro-Juárez, X.-G. Wang, T. Carrington Jr, E. Quintas-Sánchez and R. Dawes, *J. Chem. Phys.*, 2019, **151**, 084307.
33 B. Desrousseaux, E. Quintas-Sanchez, R. Dawes and F. Lique, *J. Phys. Chem. A*, 2019, **123**, 9637.
34 C. T. Bop, F. A. Batista-Romero, A. Faure, E. Quintas-Sánchez, R. Dawes and F. Lique, *ACS Earth Space Chem.*, 2019, **3**, 1151.
35 E. Quintas-Sánchez, R. Dawes, X.-G. Wang and T. Carrington Jr, *Phys. Chem. Chem. Phys.*, 2020, **22**, 22674.
36 B. Desrousseaux, E. Quintas-Sánchez, R. Dawes, S. Marinakis and F. Lique, *J. Chem. Phys.*, 2021, **154**, 034304.
37 M. Gancewski, H. Jóźwiak, E. Quintas-Sánchez, R. Dawes, F. Thibault and P. Wcisło, *J. Chem. Phys.*, 2021, **155**, 124307.
38 C. Balança, E. Quintas-Sánchez, R. Dawes, F. Dumouchel, F. Lique and N. Feautrier, *Mon. Not. R. Astron. Soc.*, 2021, **508**, 1148.
39 E. Quintas-Sánchez, R. Dawes and O. Denis-Alpizar, *Mol. Phys.*, 2021, **119**, e1980234.
40 E. Quintas-Sánchez and R. Dawes, *J. Chem. Inf. Model.*, 2019, **59**, 262.
41 R. Dawes and E. Quintas-Sánchez, *Reviews in Computational Chemistry*, 2018, ch. 5, vol. 31, pp. 199–264.
42 M. Majumder, S. A. Ndengue and R. Dawes, *Mol. Phys.*, 2016, **114**, 1.
43 R. Dawes, X.-G. Wang, A. W. Jasper and T. Carrington Jr, *J. Chem. Phys.*, 2010, **133**, 134304.
44 I. M. Sobol, *USSR Comput. Math. Math. Phys.*, 1976, **16**, 236.
45 J. Brown, X.-G. Wang, R. Dawes and T. Carrington Jr, *J. Chem. Phys.*, 2012, **136**, 134306.
46 R. Dawes, X.-G. Wang and T. Carrington Jr, *J. Phys. Chem. A*, 2013, **117**, 7612.
47 X.-G. Wang, T. Carrington Jr and R. Dawes, *J. Mol. Spectrosc.*, 2016, **330**, 179.
48 J. Brown, X.-G. Wang, T. Carrington Jr, G. S. Grubbs and R. Dawes, *J. Chem. Phys.*, 2014, **140**, 114303.
49 H. Cybulski, C. Henriksen, R. Dawes, X.-G. Wang, N. Bora, G. Avila, T. Carrington Jr and B. Fernández, *Phys. Chem. Chem. Phys.*, 2018, **20**, 12624.
50 R. Dawes, X.-G. Wang, A. W. Jasper and T. Carrington Jr, *J. Chem. Phys.*, 2010, **133**, 134304.

51 G. Donoghue, X.-G. Wang, R. Dawes and T. Carrington Jr, *J. Mol. Spectrosc.*, 2016, **330**, 170.
52 K. M. Walker, F. Dumouchel, F. Lique and R. Dawes, *J. Chem. Phys.*, 2016, **145**, 024314.
53 C. T. Bop, F. A. Batista-Romero, A. Faure, E. Quintas-Sánchez, R. Dawes and F. Lique, *ACS Earth Space Chem.*, 2019, **3**, 1151.
54 A. Barclay, A. McKellar, N. Moazzen-Ahmadi, R. Dawes, X.-G. Wang and T. Carrington Jr, *Phys. Chem. Chem. Phys.*, 2018, **20**, 14431.
55 M. Bartolomei, E. Carmona-Novillo, M. I. Hernandez, J. Campos-Martinez and R. J. Moszynski, *J. Phys. Chem. A*, 2014, **118**, 6584.
56 M. Bartolomei, E. Carmona-Novillo, M. I. Hernández, J. Campos-Martínez and R. Hernández-Lamoneda, *J. Chem. Phys.*, 2010, **133**, 124311.
57 P. S. Żuchowski, *Chem. Phys. Lett.*, 2008, **450**, 203.
58 Y. Ajili, T. Trabelsi, O. Denis-Alpizar, T. Stoecklin, A. G. Csaszar, M. Mogren Al-Mogren, J. S. Francisco and M. Hochlaf, *Phys. Rev. A*, 2016, **93**, 052514.
59 H. Ran, Y. Zhou and D. Xie, *J. Chem. Phys.*, 2007, **126**, 204304.
60 D. G. A. Smith, *et al.*, *J. Chem. Theory Comput.*, 2018, **14**, 3504.
61 J. F. Gonthier and D. C. Sherrill, *J. Chem. Phys.*, 2016, **145**, 134106.
62 A. J. Misquitta, R. Podeszwa, B. Jeziorski and K. Szalewicz, *J. Chem. Phys.*, 2005, **123**, 214103.
63 P. S. Żuchowski, B. Bussery-Honvault, R. Moszynski and B. Jeziorski, *J. Chem. Phys.*, 2003, **119**, 10497.
64 T. H. Dunning, *J. Chem. Phys.*, 1989, **90**, 1007.
65 R. A. Kendall, T. H. Dunning and R. J. Harrison, *J. Chem. Phys.*, 1992, **96**, 6796.
66 K. P. Huber and G. Herzberg, Molecular Spectra and Molecular Structure, *Constants of Diatomic Molecules*, Van Nostrand Reinhold, Wokingham, 1979, vol. IV.
67 G. Herzberg, Molecular Spectra and Molecular Structure, *Electronic Spectra and Electronic Structure of Polyatomic Molecules*, Van Nostrand, Princeton, NJ, 1966, vol. III.
68 A. E. Edwards and W. E. Roseveare, *J. Am. Chem. Soc.*, 1942, **64**, 2816.
69 R. A. Gorski and J. G. Miller, *J. Am. Chem. Soc.*, 1953, **75**, 550.
70 T. L. Cottrell, R. A. Hamilton and R. P. Taubinger, *Trans. Faraday Soc.*, 1956, **52**, 1310.
71 M. L. Martin, R. D. Trengove, K. R. Harris and P. J. Dunlop, *Aust. J. Chem.*, 1982, **35**, 1525.
72 B. Schramm and A. Buchner, *Chem. Phys. Lett.*, 1983, **98**, 118.
73 M. Jaeschke, H.-M. Hinze, H. J. Achtermann and G. Magnus, *Fluid Phase Equilib.*, 1991, **62**, 115.
74 J.-P. Crusius, R. Hellmann, J. C. Castro-Palacio and V. Vesovic, *J. Chem. Phys.*, 2018, **148**, 214306.
75 Y. Ajili, K. Hammami, N. E. Jaidane, M. Lanza, Y. N. Kalugina, F. Lique and M. Hochlaf, *Phys. Chem. Chem. Phys.*, 2013, **15**, 10062.